nature physics

ARTICLES

https://doi.org/10.1038/s41567-018-0280-z

Multiple topological states in iron-based superconductors

Peng Zhang[1*], Zhijun Wang[2], Xianxin Wu[3], Koichiro Yaji[1], Yukiaki Ishida[1], Yoshimitsu Kohama[1], Guangyang Dai[4], Yue Sun[1,5], Cedric Bareille[1], Kenta Kuroda[1], Takeshi Kondo[1], Kozo Okazaki[1], Koichi Kindo[1], Xiancheng Wang[4], Changqing Jin[4], Jiangping Hu[4,6], Ronny Thomale[3], Kazuki Sumida[7], Shilong Wu[8], Koji Miyamoto[8], Taichi Okuda[8], Hong Ding[4,6], G. D. Gu[9], Tsuyoshi Tamegai[5], Takuto Kawakami[10], Masatoshi Sato[10] and Shik Shin[1*]

Topological materials and unconventional iron-based superconductors are both important areas of study but, to date, relatively little overlap has been identified between these two fields. However, the combination of topological bands and superconductivity promises the manifestation of exotic superconducting states, including Majorana fermions, the central component of topological quantum computation. Here, using laser-based, spin-resolved and angle-resolved photoemission spectroscopy and density functional theory calculations, we have identified both topological insulator and Dirac semimetal states near the Fermi energy in different iron-based superconducting compounds. Carrier doping can tune these topologically non-trivial bands to the Fermi energy, potentially allowing access to several different superconducting topological states in the same material. These results reveal the generic coexistence of superconductivity and multiple topological states in iron-based superconductors, indicating that this broad class of materials is a promising platform for high-temperature topological superconductivity.

Iron-based superconductors with high critical temperature (T_c) feature multiple bands near the Fermi energy (E_F), which makes understanding the details of unconventional pairing more difficult[1–3]. However, it also allows for a wealth of, possibly topologically non-trivial[4–7], electronic states, of which a recent example is the topological insulator (TI) states discovered[8] in the iron-based superconductor Fe(Te,Se), hinting at a promising direction to realize topological superconductivity and Majorana bound states[9–13]. In this work, we show that this initial finding is only one facet of the rich scope of combined topology and unconventional superconductivity: different types of topological states (both insulator and semimetal) coexist with unconventional high-T_c superconductivity, which is a generic feature of various iron-based superconductors. First, we predict and observe that TI bands reminiscent of Fe(Te,Se) exist in Li(Fe,Co)As as well, indicating that TI states appear in various iron-based superconductors. Second, and more interestingly, we predict and observe topological Dirac semimetal (TDS) bands in Li(Fe,Co)As and Fe(Te,Se), supported by high-resolution angle-resolved photoemission spectroscopy (ARPES), spin-resolved ARPES (SARPES) and magnetoresistance measurements, proving the generic existence of different types of topological states in iron-based superconductors. Finally, the phase diagram of these superconducting topological states as a function of doping is discussed. The combination of topological states and high-T_c unconventional superconductivity may produce not only surface topological superconductivity deriving from the TI edge states, but also bulk topological superconductivity from the TDS bands.

Normal insulator, TI and TDS constitute topologically distinct phases[14–17]. From a band structure point of view, if there is no band inversion in the entire Brillouin zone, the material will be a normal insulator, with no spin-polarized surface states, as shown in Fig. 1a. In a simple case, if there is a single band inversion in the entire Brillouin zone, the material will be topologically non-trivial, with spin-polarized Dirac-cone type bands. In a TI, the bulk bandgap leads to well-defined surface states, with explicit spin helicity (Fig. 1b). Instead, in a TDS, the band crossing is protected by the crystal symmetry. There are still surface states, but these generally overlap with the bulk states on the (001) surface[16–21], as indicated by the spin-polarized spectrum in Fig. 1c. The spin helicity of the surface states may not be fixed (Supplementary Information Part 6). The spin-polarization magnitudes of the (001) surface states generally show a gradual increase with increased distance from the Dirac point. The three phases may coexist in one material.

In Fe(Te,Se) the band inversion near E_F occurs only along the k_z direction between the p_z and d_{xz}/d_{yz} bands, responsible for the non-trivial topological invariance[5,8]. Here we further check the band structure of the four major classes of iron-based superconductors, focusing on the only possible band inversion of p_z and d_{xz}/d_{yz} bands, which is directly related to the topology. The separations between the adjacent FeAs/FeSe layers Δ_d are 8.741, 6.508, 6.364 and 5.955 Å for LaOFeAs (1111), $BaFe_2As_2$ (122), LiFeAs (111) and $FeTe_{0.5}Se_{0.5}$ (11), respectively[2,5]. This separation directly determines the interlayer *pp* coupling, which will affect the bandwidth of the p_z band

[1]Institute for Solid State Physics, University of Tokyo, Kashiwa, Japan. [2]Department of Physics, Princeton University, Princeton, NJ, USA. [3]Institut für Theoretische Physik und Astrophysik, Julius-Maximilians-Universität Würzburg, Würzburg, Germany. [4]Beijing National Laboratory for Condensed Matter Physics and Institute of Physics, Chinese Academy of Sciences, Beijing, China. [5]Department of Applied Physics, University of Tokyo, Tokyo, Japan. [6]CAS Center for Excellence in Topological Quantum Computation, University of Chinese Academy of Sciences, Beijing, China. [7]Graduate School of Science, Hiroshima University, Higashi-Hiroshima, Japan. [8]Hiroshima Synchrotron Radiation Center, Hiroshima University, Higashi-Hiroshima, Japan. [9]Condensed Matter Physics and Materials Science Department, Brookhaven National Laboratory, Upton, NY, USA. [10]Yukawa Institute for Theoretical Physics, Kyoto University, Kyoto, Japan. *e-mail: zhangpeng@issp.u-tokyo.ac.jp; shin@issp.u-tokyo.ac.jp

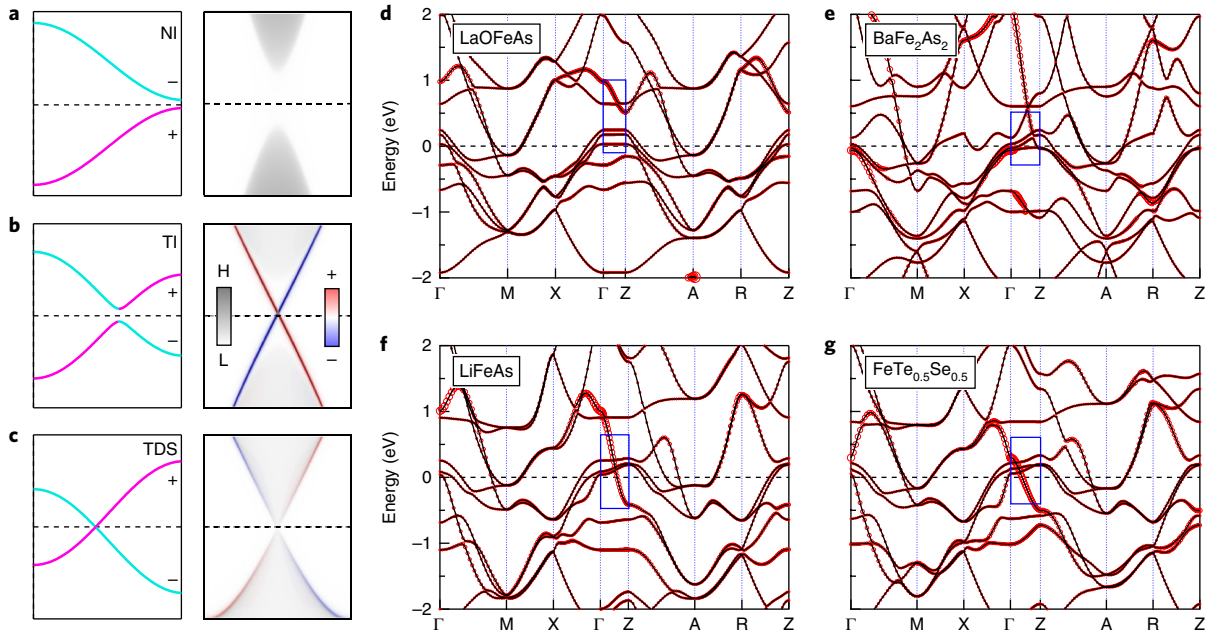

Fig. 1 | Different topological phases and band structures of iron-based superconductors. a–c, Out-of-plane dispersion and the corresponding (001) surface spectrum, for normal insulator (NI) (**a**), TI (**b**) and TDS (**c**). We overlapped the spin-polarized surface spectrum (blue and red) on top of the spin-integrated surface spectrum (grey). H, high intensity; L, low intenstiy. **d–g**, Band structures of LaOFeAs, $BaFe_2As_2$, LiFeAs and $FeTe_{0.5}Se_{0.5}$, respectively. The size of the red circles represent the weights of the As/Se p_z orbital. No band inversion between p_z and d_{xz}/d_{yz} is found in LaOFeAs, whereas there are band inversions in $BaFe_2As_2$, LiFeAs and $FeTe_{0.5}Se_{0.5}$.

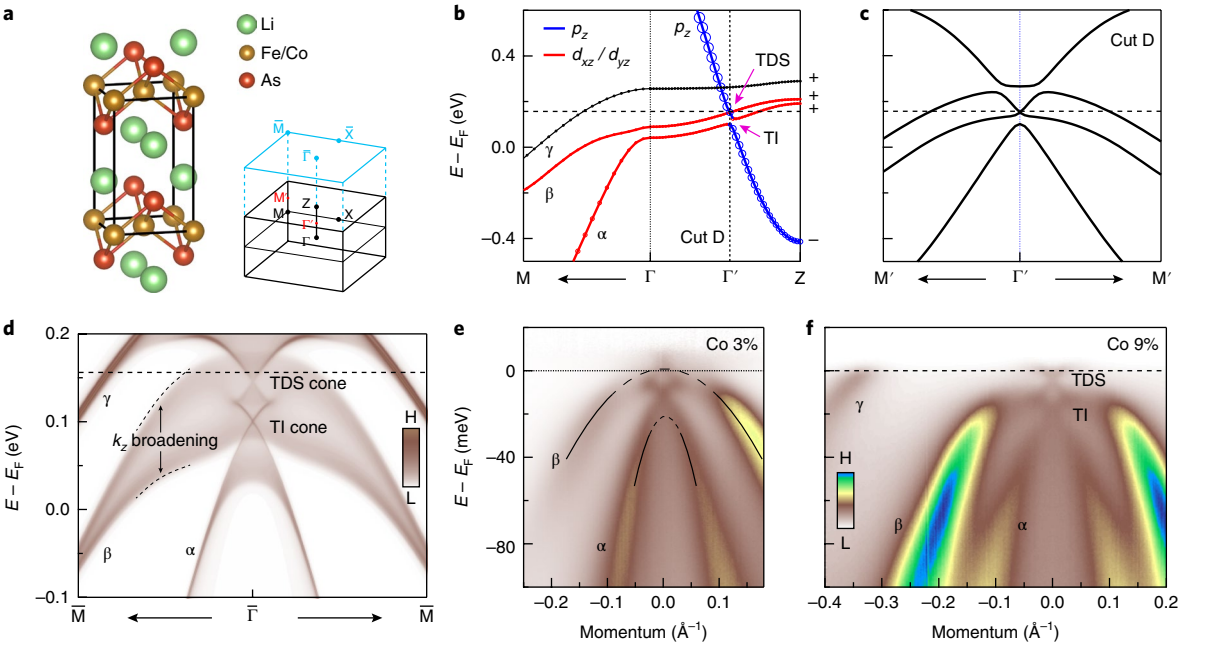

Fig. 2 | Electronic structure of Li(Fe,Co)As. a, Left: crystal structure of Li(Fe,Co)As. Right: high-symmetry points in the 3D Brillouin zone and (001) surface Brillouin zone. **b,** Zoomed-in view of the LiFeAs band dispersion along ΓM and ΓZ. Red indicates the d_{xz}/d_{yz} bands and blue indicates the p_z band. The marker size relates to the weight of the p_z orbital character. The avoided crossing between the p_z and α bands produces TI states, whereas the real crossing between the p_z and β bands produces TDS states. The crossing between the p_z and γ bands also produces TDS states far above E_F. **c**, In-plane band structure at Cut D, where the bulk Dirac cone of the TDS bands is shown. **d**, (001) surface spectrum of LiFeAs. There is a large broadening in the spectrum at the α and β band tops with reduced intensity, due to the k_z dispersion. **e**, ARPES intensity plot of $LiFe_{1-x}Co_xAs$ ($x = 3\%$) at 15 K, with a laser delivering p-polarized 7-eV photons. The spectrum is divided by the corresponding Fermi function. **f**, ARPES intensity plot of $LiFe_{1-x}Co_xAs$ ($x = 9\%$) at 10 K, with p-polarized 7-eV photons. The two Dirac cones are similar to the ones in the calculation (**d**).

along ΓZ (ref.[5]). The parameter Δ_d of LaOFeAs is much larger than that of $BaFe_2As_2$, LiFeAs and Fe(Te,Se), resulting in a small p_z dispersion for LaOFeAs but large p_z dispersions for $BaFe_2As_2$, LiFeAs and Fe(Te,Se). In Fig. 1d–g, we show the band structures of the four classes. It is clear that along the ΓZ direction there is no band inversion for LaOFeAs, whereas there are band inversions for $BaFe_2As_2$,

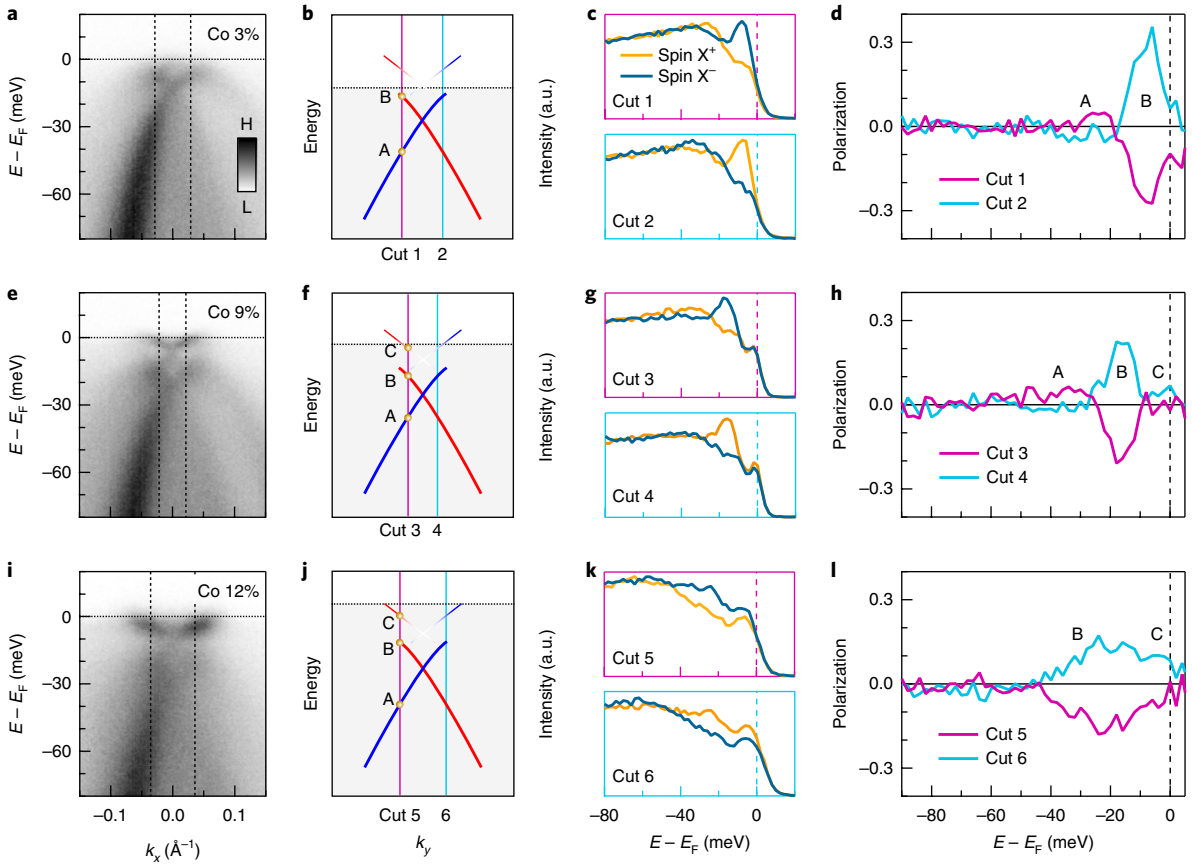

Fig. 3 | Spin polarization of the surface Dirac cones from the TI and TDS states in Li(Fe$_{1-x}$Co$_x$)As. a, Intensity plot along k_x for the $x = 3\%$ sample, with *p*-polarized 7-eV photons. **b**, Sketch of the spin-polarized surface bands along k_y. The blue and red lines stand for opposite spin polarizations, as confirmed by the data in **c**, **d**. We measured spin-resolved energy distribution curves at the cuts indicated by pink (Cut 1) and cyan (Cut 2) lines. The two lines are also duplicated in **a** as dashed lines. Note that the two cuts in **b** are at different k_y, to avoid the intensity asymmetry along k_x in **a** (Supplementary Information Part 1). The band structures along k_y and k_x are the same because of the crystal symmetry. **c**, Spin-resolved energy distribution curves at Cut 1 (top) and Cut 2 (bottom), respectively. **d**, Spin polarization at Cut 1 and Cut 2. The spin along the *x* direction is measured. A and B correspond to the positions indicated in **b**. **e**–**h**, Same as **a**–**d**, but for samples with $x = 9\%$. **i**–**l**, same as **a**–**d**, but for samples with $x = 12\%$.

LiFeAs and Fe(Te,Se). In two-dimensional (2D) thin films, such as Fe(Te,Se) monolayer films, there is no k_z dispersion. However, the band inversion may still occur for the in-plane band structure. The in-plane lattice parameter *a* (or Se/Te height) affects the intralayer *pd* coupling and determines the position of the p_z band at Γ. By reducing the parameter *a* (increasing the Se/Te height), the p_z band will sink below the $d_{xz/yz}$ band at Γ, generating a band inversion and realizing a 2D topological insulator[6,22,23].

Band structure measurements are required to verify the existence of the non-trivial topology. Since LiFeAs has no magnetic and structural transitions compared to $BaFe_2As_2$, we carried out a detailed study on the band structure of Li(Fe,Co)As (refs [24–27]). Although there are reports on the p_z band in LiFeAs and NaFeAs[5,28], no evidence of the topological bands is observed due to the low resolution. The high-resolution laser-based ARPES makes it possible to resolve the topological bands and confirm the topological nature. The crystal structure of Li(Fe,Co)As is shown in Fig. 2a. The Li atoms are fairly close to the FeAs plane, resulting in a lattice parameter *c* comparable to that of Fe(Te,Se). Thus a large p_z dispersion is also present in LiFeAs, as shown in the zoomed-in view of the band structure along k_z in Fig. 2b. The spin–orbit coupling splits the d_{xz}/d_{yz} bands, forming two hybridized bands α and β, which both have mixed d_{xz}/d_{yz} orbitals along k_z. When the p_z band with odd parity ('−') crosses the α band with even parity ('+'), band inversion is formed. The spin–orbit coupling produces an avoided crossing between the p_z and α bands, resulting in TI states, similar to that of Fe(Te,Se) (ref. [8]). We further notice that the β band also has an even parity ('+'). The crossing between the p_z and β bands is protected by the crystal C_4 rotation symmetry, and forms a three-dimensional (3D) Dirac cone. Consequently, the band inversion and the protected band crossing produce TDS states. At the cut of the Dirac point (Cut D in Fig. 2b), the in-plane bulk Dirac cone of the TDS bands is evident in the band structure, as shown in Fig. 2c. Both TI and TDS states can be visualized at the same time in the (001) surface spectrum (Fig. 2d). Consistent with the two band inversions in Fig. 2b, the TI surface states form the lower Dirac cone, and the TDS surface states form the upper Dirac cone. The bulk states with large k_z dispersion appear as broad and weak continuums and thus the bulk Dirac cone of the TDS states is not apparent in the surface spectrum.

By changing the Fermi level by means of different Co content, we observed both TI and TDS Dirac cones in Li(Fe,Co)As at the same time. The ARPES band structure of Li(Fe,Co)As with 3% Co is shown in Fig. 2e. Despite the Dirac cone from the TI bands, the second Dirac cone from the TDS states, which is above E_F, shows up in the ARPES spectrum divided by the corresponding Fermi function. We further checked the Li(Fe,Co)As sample with 9% Co (shown in Fig. 2f). As expected, the TDS cone shifts down and the full cone clearly shows up, directly confirming the existence of the TDS states. We notice that the parabolic band tops of the α and β bulk bands are missing or too broad to distinguish in Fig. 2e,f, showing

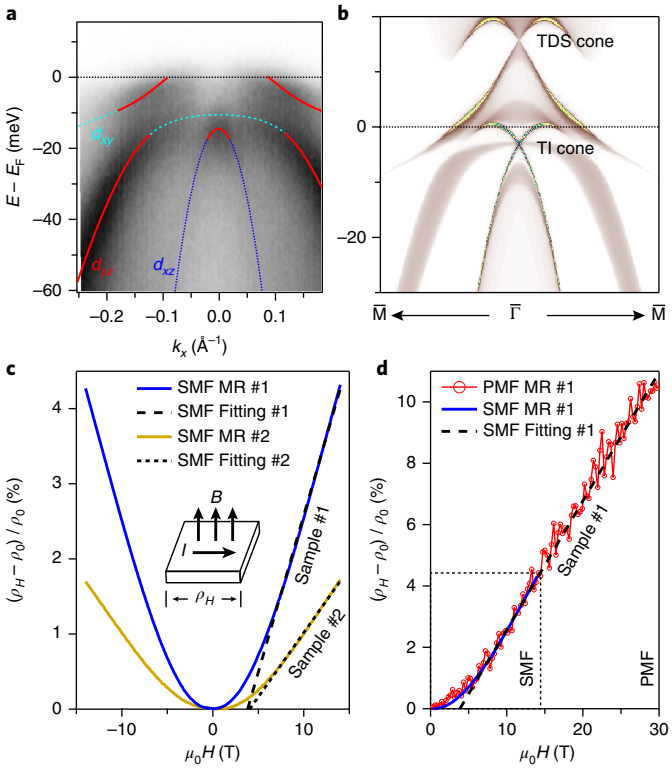

Fig. 4 | The TDS bands in Fe(Te,Se) and the linear magnetoresistance. **a**, ARPES intensity plot of the band structure measured with *s*-polarized 7-eV photons. Note that the TI surface Dirac band appears with *p*-polarized photons, as shown in Supplementary Fig. 5. **b**, Calculated (001) surface spectrum based on the $\mathbf{k}\cdot\mathbf{p}$ model. **c**, Magnetoresistance (MR) measured on two different Fe(Te,Se) samples in a static magnetic field (SMF) up to 14 T. Solid curves are the experimental results, and dashed lines are linear fittings of the magnetoresistance curves in the range 6–14 T. The different magnetoresistance values of the two samples may come from magnetic scattering by different contents of excess Fe (ref. [50]). **d**, Magnetoresistance measured in a pulsed magnetic field (PMF) up to 30 T. The red curve represents the data from the pulsed field measurements. The blue solid curve and black dashed line are duplicates of the static field results on sample #1 in **c**. Both magnetoresistance experiments were carried out at 16 K.

similar spectral features to the calculated surface spectrum, which indicates a strong k_z broadening effect in the laser-ARPES data[29]. Due to the strong k_z broadening effect, the p_z bulk continuum will be very broad and thus the two sharp Dirac cones in Fig. 2e,f should come from surface states.

The surface Dirac cones of the TI and TDS states should both be spin-polarized, as shown in Fig. 1b,c. Thus we can use SARPES[30] to check their surface nature. In Fig. 3 we show the data on three different compositions of $LiFe_{1-x}Co_xAs$. The spin-integrated band structures are the same as the ones in Fig. 2, except for some intensity difference induced by the experimental geometries (Supplementary Information Part 1). A pair of spin-polarized energy distribution curves along k_y was measured, with their positions illustrated in Fig. 3b,f,j. We first focus on the spin polarization of the TI Dirac cone, which is obtained from both $x = 3\%$ and $x = 9\%$ samples, and shown in Fig. 3a–h. In both samples, the lower part of the cone (position A) shows the opposite spin polarization to the upper part (position B), and the left-hand part of the cone (Cut 1 and Cut 3) shows the opposite spin polarization to the right-hand part (Cut 2 and Cut 4), as expected for the spin polarization from a Dirac cone. The direction of the spin polarization indicates that the Dirac cone has a left-hand helicity, the same as that of Fe(Te,Se) and most TIs (see also Supplementary Information Part 2). As we discussed in connection with Fig. 1, the TDS surface Dirac cone is similar to that of TI, whose spin polarization can be obtained from both the $x = 9\%$ and $x = 12\%$ samples, as shown in Fig. 3e–l. Since the lower part of the TDS surface cone shows a very weak intensity (Fig. 3e,i), we focus on the spin polarization of the upper part (position C). In the $x = 9\%$ sample (Fig. 3g,h), a weak spin polarization at position C is resolved. In the $x = 12\%$ sample (Fig. 3k,l), a pair of energy distribution curves more distant from the conical point is measured and a larger spin polarization is observed. These results are consistent with the model calculations in Fig. 1c: the magnitude of the spin polarization of the TDS surface cone is smaller near the conical point and larger far from the conical point. The experimental spin polarizations of the TI and TDS surface cones are summarized in Fig. 3b,f,j. The spin polarizations confirm that the two Dirac cones indeed come from the surface states.

Because of the similar band structure of Li(Fe,Co)As and Fe(Te,Se), the TDS states may also exist in Fe(Te,Se). The detailed band structure of Fe(Te,Se) from high-resolution ARPES is shown in Fig. 4a and Supplementary Information Part 4 and 5. The d_{xy} orbital is below the d_{yz} orbital at the Γ point, and a hybridization gap opens at their crossing points, similar to the case of FeSe (refs [31,32]), but slightly different from the density functional theory calculations. Thus, a $\mathbf{k}\cdot\mathbf{p}$ model based on the real band structure is built to describe the topological states more accurately (Supplementary Information Part 5). The TDS bands are clearly shown in the (001) surface spectrum in Fig. 4b. Since there is no mixing of the TDS states and other bulk states near Γ, evidence of the TDS states may appear in the transport measurements. It is well known that Dirac and Weyl semimetals, which host bulk Dirac bands, generically show a magnetoresistance that is linearly dependent on the magnetic field[17,33,34], which can be explained by the quantum magnetoresistance[35]. If there are TDS bands near E_F in Fe(Te,Se), it is very likely that such a linear magnetoresistance should also be realized, the measurement of which we report in the following. The magnetoresistance was measured at 16 K on two batches of samples (samples #1 and #2) with different growth methods (see Methods). Both samples show similar magnetoresistance curves in a static magnetic field, as shown in Fig. 4c. Indeed, the magnetoresistance curve above 6 T shows a quantum linear behaviour, whereas the curve below 6 T exhibits a semiclassical quadratic dispersion. The linear fitting in the range 6–14 T matches well with the experimental curve. We also checked the magnetoresistance in pulsed high magnetic fields up to 30 T on sample #1, and show the results in Fig. 4d. The magnetoresistance in pulsed fields in the range 0–14 T is the same as that measured in static fields. Above 14 T, the pulsed-field magnetoresistance exactly follows extrapolation of the linear fitting of the magnetoresistance in the static field. All these results clearly show the existence of linear magnetoresistance above 6 T in Fe(Te,Se). We note that there are reports of topologically trivial bulk Dirac bands near the M point in magnetic $BaFe_2As_2$ (ref. [36]) or nematic FeSe (ref. [37]). In contrast, however, in Fe(Te,Se) there is no report of such orders, and no Dirac cone was observed[38,39]. Thus, this linear magnetoresistance most likely comes from the TDS bands.

We also obtain evidence of the TDS bands in Fe(Te,Se) by measuring the associated surface states. Although they generally overlap with bulk states on the (001) surface, their spin-polarized character provides a unique signature to those surface states, detectable via spin-resolved photoemission measurements, as already shown in Fig. 3. The intensity plots of Fe(Te,Se) from SARPES are shown in Fig. 5a,b. The spin-integrated plot is the same as the one in Fig. 4a, showing clearly the hybridization of d_{xy} and d_{yz} obitals, whereas the spin-resolved intensity plot (the intensity difference between spin-up and spin-down photoelectrons) shows the spin polarization of the d_{yz} band near E_F. As shown in the inset of Fig. 5c, we measured four cuts, with all four spin-resolved energy distribution

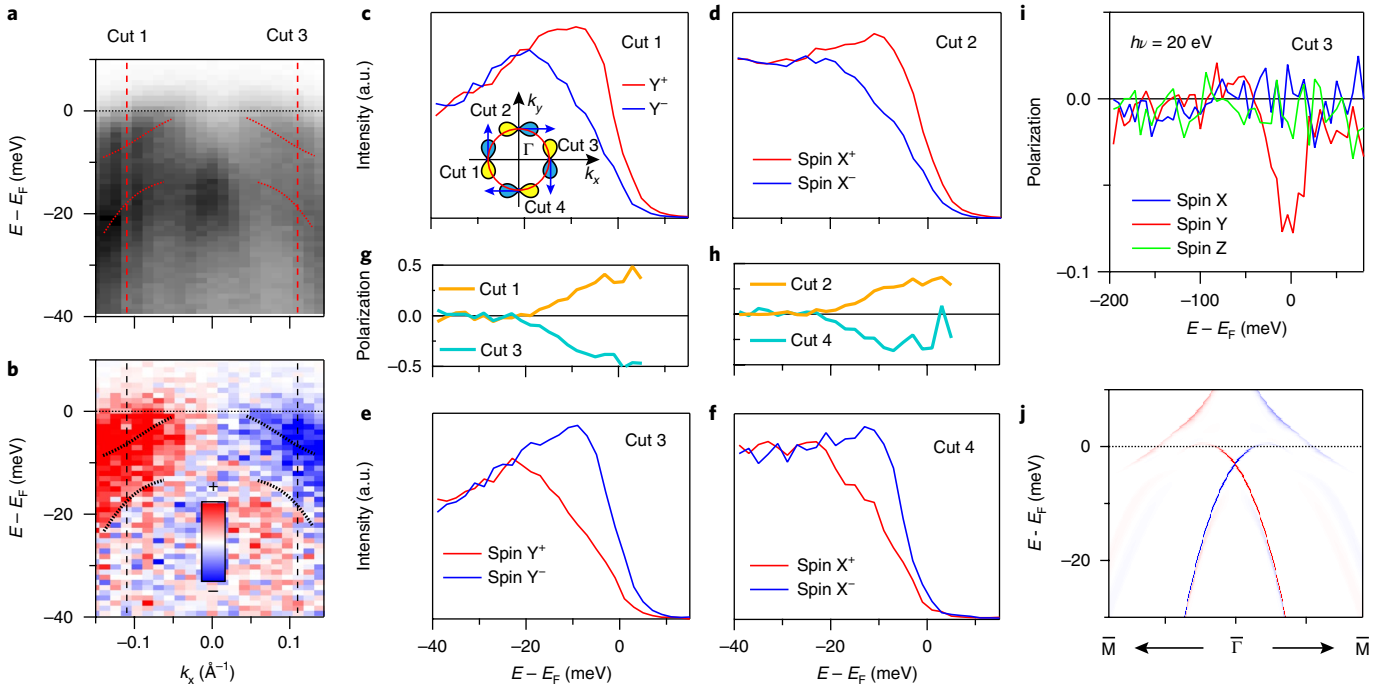

Fig. 5 | Spin polarization of the d_{yz} band in Fe(Te,Se). a,**b**, Spin-resolved intensity plot at Γ with *s*-polarized 7-eV photons. The intensity scales the sum (**a**) or difference (**b**) of spin-up and spin-down photoelectrons along the *y* direction. **c**–**f**, Spin-resolved energy distribution curves at Cuts 1–4. Cuts 1 and 3 are taken with *s*-polarized photons, whereas Cuts 2 and 4 are taken with *p*-polarized photons, due to the matrix element effect. The inset of **c** shows the positions of the four cuts, and the spin directions are extracted from **g**,**h**. **g**,**h**, Spin-polarization curves at Cuts 1–4. **i**, The spin polarization along the *x*, *y* and *z* diretions at Cut 3 measured with 20-eV photons from synchrotron radiation. **j**, Spin-resolved (001) surface spectrum calculated from the **k**·**p** model.

curves (Fig. 5c–f) show clear spin polarizations (Fig. 5g,h), exhibiting a helical texture. To further confirm that the spin polarizations are the intrinsic properties of the electronic states in the crystal and not induced by the photoemission process, we also checked the spin polarization with different photon energies in a synchrotron facility, as shown in Fig. 5i, and with different photon polarizations, as shown in Supplementary Information Part 8. All the results consistently show a spin-helical texture, excluding the possibility that the spin polarizations come from the photoelectron process or spin matrix-element effect. The magnitude of spin polarization of the d_{yz} band is about 50%, indicating coexistence of unpolarized bulk and polarized surface states. The results are consistent with the spin-resolved spectrum from calculations, as shown in Fig. 5j.

The coexistence of TI and TDS bands near the Fermi level in iron-based superconductors provides the basis for a rich variety of possible topologically superconducting states. Based on the band structure of Fe(Te,Se), the right-hand side of Fig. 6a illustrates the possible superconducting states as one were to shift E_F to the TI or TDS Fermi level region via charge carrier doping. In both the TI and TDS regions, spin-helical Fermi surfaces are expected for the surface states. For the TDS, the spin-helical Fermi surfaces (Fermi arc pairs) appear on some side surfaces[16,40], with two spherical bulk Fermi surfaces along the ΓZ line, as shown in Fig. 6b. Invoking the notion that spin-helical surface states in proximity to a bulk *s*-wave superconductor feature topologically superconducting states with Majorana bound states in its associated vortex cores[9], the surface states in the TI region are expected to exhibit topological superconductivity, which is already observed by ARPES and scanning tunnelling microscopy measurements[8,41]. Similarly, if bulk *s*-wave pairing persists in the TDS region, the spin-helical Fermi surfaces on side surfaces are likewise expected to form topologically superconducting states (Fig. 6b). However, since *d* orbitals dominate the Fermi level density of states in iron-based superconductors and exhibit strong correlation effects such as Hund's coupling, the inter-orbital pairing may dominate in the TDS Fermi level region, which would generate a spin triplet pairing state on the two spherical bulk Fermi surfaces with point nodes on the k_z axis (Fig. 6c), as a consequence of orbit–momentum locking in the bulk Dirac cone[42,43]. Such a scenario would hence yield yet another intriguing pairing state, namely a bulk topological superconductor[42–44], which would host Majorana fermions on its side surfaces. Since few reports on the observation of intrinsic superconductivity within TDSs are available, except certain evidence of superconductivity in Cd_3As_2 induced by a point contact or external pressure[45–47], the TDS states in iron-based high-T_c superconductors provide a unique platform for studies on such bulk topological superconductivity.

A shift of the Fermi level could also induce a topological phase transition from topological superconductor to trivial superconductor[7], which might be useful to optimize the conditions for surface topological superconductivity and Majorana bound states. It is, however, difficult to study such proposals in the scope of Fe(Te,Se), as it appears tedious to change the electron doping of Fe(Te,Se) without noticeably affecting the coherence of the electronic states. Fortunately, the Fermi level of Li(Fe,Co)As is easily tuned by the Co content, and the TI/TDS bands may be separately accessed, rendering Li(Fe,Co)As ideal for such studies. One important aspect to address is the overlapping character between the trivial bulk states and the topological bands, which might interfere with the topological pairing, or might stabilize topological superconductivity over a greater range of doping[48,49]. We defer a more detailed discussion of these issues to future work.

Our findings of the TI and TDS states in Li(Fe,Co)As and Fe(Te,Se) prove the generic existence of different types of topological states in iron-based superconductors. Their simple structures, multiple topological states, and a tunable Fermi level make iron-based superconductors ideal platforms for the study of topological

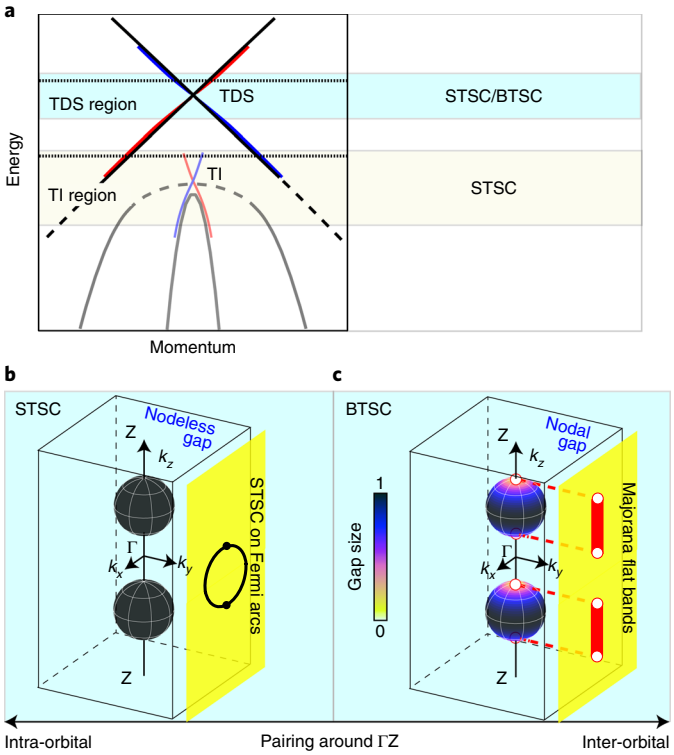

Fig. 6 | Topological states and the related topological superconductivity. **a**, Sketch of the in-plane band structure of Fe(Te,Se). There will be surface topological superconductivity (STSC) or bulk topological superconductivity (BTSC) if E_F is located in the corresponding region. **b**,**c**, In the case that E_F located in the TDS region, there will be two spherical Fermi surfaces along ΓZ: if the intra-orbital pairing around ΓZ dominates (**b**), the superconducting gap will be nodeless and the Fermi arcs on side surfaces will be topologically superconducting, whereas if the inter-orbital pairing around ΓZ dominates (**c**), the superconducting gap will be isotropic in plane and have nodes along k_z. In this case, there is topological superconductivity in the bulk and Majorana fermions on side surfaces.

superconductivity, Majorana bound states, and as such, potentially, topological quantum computation.

Online content

Any methods, additional references, Nature Research reporting summaries, source data, statements of data availability and associated accession codes are available at https://doi.org/10.1038/s41567-018-0280-z.

Received: 9 April 2018; Accepted: 20 August 2018;
Published online: 24 September 2018

References

1. Kamihara, Y., Watanabe, T., Hirano, M. & Hosono, H. Iron-based layered superconductor La[$O_{1-x}F_x$]FeAs (x=0.05–0.12) with T_c = 26 K. *J. Am. Chem. Soc.* **130**, 3296–3297 (2008).
2. Johnston, D. C. The puzzle of high temperature superconductivity in layered iron pnictides and chalcogenides. *Adv. Phys.* **59**, 803–1061 (2010).
3. Stewart, G. R. Superconductivity in iron compounds. *Rev. Mod. Phys.* **83**, 1589–1652 (2011).
4. Hao, N. & Hu, J. Topological phases in the single-layer FeSe. *Phys. Rev. X* **4**, 031053 (2014).
5. Wang, Z. et al. Topological nature of the $FeSe_{0.5}Te_{0.5}$ superconductor. *Phys. Rev. B* **92**, 115119 (2015).
6. Wu, X., Qin, S., Liang, Y., Fan, H. & Hu, J. Topological characters in Fe($Te_{1-x}Se_x$) thin films. *Phys. Rev. B* **93**, 115129 (2016).
7. Xu, G., Lian, B., Tang, P., Qi, X.-L. & Zhang, S.-C. Topological superconductivity on the surface of Fe-based superconductors. *Phys. Rev. Lett.* **117**, 047001 (2016).
8. Zhang, P. et al. Observation of topological superconductivity on the surface of an iron-based superconductor. *Science* **360**, 182–186 (2018).
9. Fu, L. & Kane, C. L. Superconducting proximity effect and Majorana fermions at the surface of a topological insulator. *Phys. Rev. Lett.* **100**, 096407 (2008).
10. Mourik, V. et al. Signatures of Majorana fermions in hybrid superconductor–semiconductor nanowire devices. *Science* **336**, 1003–1007 (2012).
11. Nadj-Perge, S. et al. Observation of Majorana fermions in ferromagnetic atomic chains on a superconductor. *Science* **346**, 602–607 (2014).
12. Albrecht, S. M. et al. Exponential protection of zero modes in Majorana islands. *Nature* **531**, 206–209 (2016).
13. Zhang, F., Kane, C. L. & Mele, E. J. Time-reversal-invariant topological superconductivity and Majorana Kramers pairs. *Phys. Rev. Lett.* **111**, 056402 (2013).
14. Hasan, M. Z. & Kane, C. L. Colloquium: topological insulators. *Rev. Mod. Phys.* **82**, 3045–3067 (2010).
15. Qi, X.-L. & Zhang, S.-C. Topological insulators and superconductors. *Rev. Mod. Phys.* **83**, 1057–1110 (2011).
16. Wang, Z. et al. Dirac semimetal and topological phase transitions in A_3Bi (A = Na, K, Rb). *Phys. Rev. B* **85**, 195320 (2012).
17. Wang, Z., Weng, H., Wu, Q., Dai, X. & Fang, Z. Three-dimensional Dirac semimetal and quantum transport in Cd_3As_2. *Phys. Rev. B* **88**, 125427 (2013).
18. Liu, Z. K. et al. Discovery of a three-dimensional topological Dirac semimetal, Na_3Bi. *Science* **343**, 864–867 (2014).
19. Xu, S.-Y. et al. Unconventional transformation of spin Dirac phase across a topological quantum phase transition. *Nat. Commun.* **6**, 6870 (2015).
20. Neupane, M. et al. Surface versus bulk Dirac state tuning in a three-dimensional topological Dirac semimetal. *Phys. Rev. B* **91**, 241114 (2015).
21. Jozwiak, C. et al. Spin-polarized surface resonances accompanying topological surface state formation. *Nat. Commun.* **7**, 13143 (2016).
22. Wu, X. et al. $CaFeAs_2$: a staggered intercalation of quantum spin Hall and high-temperature superconductivity. *Phys. Rev. B* **91**, 081111 (2015).
23. Shi, X. et al. $FeTe_{1-x}Se_x$ monolayer films: towards the realization of high-temperature connate topological superconductivity. *Sci. Bull.* **62**, 503–507 (2017).
24. Wang, X. et al. The superconductivity at 18 K in LiFeAs system. *Solid State Commun.* **148**, 538–540 (2008).
25. Borisenko, S. V. et al. Superconductivity without nesting in LiFeAs. *Phys. Rev. Lett.* **105**, 067002 (2010).
26. Pitcher, M. J. et al. Compositional control of the superconducting properties of LiFeAs. *J. Am. Chem. Soc.* **132**, 10467–10476 (2010).
27. Miao, H. et al. Observation of strong electron pairing on bands without Fermi surfaces in $LiFe_{1-x}Co_xAs$. *Nat. Commun.* **6**, 124508 (2015).
28. Watson, M. D. et al. Three-dimensional electronic structure of the nematic and antiferromagnetic phases of NaFeAs from detwinned angle-resolved photoemission spectroscopy. *Phys. Rev. B* **97**, 035134 (2018).
29. Strocov, V. Intrinsic accuracy in 3-dimensional photoemission band mapping. *J. Electron. Spectrosc. Relat. Phenom.* **130**, 65–78 (2003).
30. Yaji, K. et al. High-resolution three-dimensional spin- and angle-resolved photoelectron spectrometer using vacuum ultraviolet laser light. *Rev. Sci. Instrum.* **87**, 053111 (2016).
31. Watson, M. D. et al. Emergence of the nematic electronic state in FeSe. *Phys. Rev. B* **91**, 155106 (2015).
32. Zhang, P. et al. Observation of two distinct d_{xz}/d_{yz} band splittings in FeSe. *Phys. Rev. B* **91**, 214503 (2015).
33. Liang, T. et al. Ultrahigh mobility and giant magnetoresistance in the Dirac semimetal Cd_3As_2. *Nat. Mater.* **14**, 280–284 (2014).
34. Feng, J. et al. Large linear magnetoresistance in Dirac semimetal Cd_3As_2 with Fermi surfaces close to the Dirac points. *Phys. Rev. B* **92**, 081306 (2015).
35. Abrikosov, A. A. Quantum magnetoresistance. *Phys. Rev. B* **58**, 2788–2794 (1998).
36. Richard, P. et al. Observation of Dirac cone electronic dispersion in $BaFe_2As_2$. *Phys. Rev. Lett.* **104**, 137001 (2010).
37. Tan, S. Y. et al. Observation of Dirac cone band dispersions in FeSe thin films by photoemission spectroscopy. *Phys. Rev. B* **93**, 104513 (2016).
38. Miao, H. et al. Isotropic superconducting gaps with enhanced pairing on electron Fermi surfaces in $FeTe_{0.55}Se_{0.45}$. *Phys. Rev. B* **85**, 094506 (2012).
39. Rinott, S. et al. Tuning across the BCS–BEC crossover in the multiband superconductor $Fe_{1+y}Se_xTe_{1-x}$: An angle-resolved photoemission study. *Sci. Adv.* **3**, e1602372 (2017).
40. Xu, S.-Y. et al. Observation of Fermi arc surface states in a topological metal. *Science* **347**, 294–298 (2015).
41. Wang, D. et al. Evidence for Majorana bound states in an iron-based superconductor. *Science* https://doi.org/10.1126/science.aao1797 (2018).
42. Kobayashi, S. & Sato, M. Topological superconductivity in Dirac semimetals. *Phys. Rev. Lett.* **115**, 187001 (2015).

43. Hashimoto, T., Kobayashi, S., Tanaka, Y. & Sato, M. Superconductivity in doped Dirac semimetals. *Phys. Rev. B* **94**, 014510 (2016).
44. Yang, S. A., Pan, H. & Zhang, F. Dirac and Weyl superconductors in three dimensions. *Phys. Rev. Lett.* **113**, 046401 (2014).
45. Aggarwal, L. et al. Unconventional superconductivity at mesoscopic point contacts on the 3D Dirac semimetal Cd_3As_2. *Nat. Mater.* **15**, 32–37 (2015).
46. Wang, H. et al. Observation of superconductivity induced by a point contact on 3D Dirac semimetal Cd_3As_2 crystals. *Nat. Mater.* **15**, 38–42 (2015).
47. He, L. et al. Pressure-induced superconductivity in the three-dimensional topological Dirac semimetal Cd_3As_2. *npj Quant. Mater.* **1**, 1057 (2016).
48. Hosur, P., Ghaemi, P., Mong, R. S. K. & Vishwanath, A. Majorana modes at the ends of superconductor vortices in doped topological insulators. *Phys. Rev. Lett.* **107**, 097001 (2011).
49. Chiu, C.-K., Ghaemi, P. & Hughes, T. L. Stabilization of Majorana modes in magnetic vortices in the superconducting phase of topological insulators using topologically trivial bands. *Phys. Rev. Lett.* **109**, 237009 (2012).
50. Sun, Y. et al. Multiband effects and possible Dirac fermions in $Fe_{1+y}Te_{0.6}Se_{0.4}$. *Phys. Rev. B* **89**, 144512 (2014).

Acknowledgements

We acknowledge K. Asakawa, A. Harasawa, Y. Hesagawa, D. Hirai, Z. Hiroi, K. Ishizaka, N. Mitsuishi, M. Sakano and Y. Yoshida for experimental assistance. This work was supported by the Photon and Quantum Basic Research Coordinated Development Program from MEXT, JSPS (KAKENHI Grant Nos. 25220707, JP17H02922, JP16K17755 and 17H01141), the Grants-in-Aid for Scientific Research on Innovative Areas 'Topological Material Science', JSPS (grant no. JP15H05855), the Chinese Academy of Sciences (XDB28000000) and the Ministry of Science and Technology of China (2015CB921300). The work in Brookhaven is supported by the Office of Science, US Department of Energy under contract no. DE-SC0012704 and the Center for Emergent Superconductivity, an Energy Frontier Research Center funded by the US Department of Energy, Office of Science. The work in Würzburg is supported by ERC-StG-TOPOLECTRICS-336012, DFG-SFB 1170 and DFG-SPP 1666.

Author contributions

P.Z. performed the ARPES measurements on Li(Fe,Co)As and analysed the data with help from K.Y., T. Kondo and S.S.. X. Wu, J.H. and R.T. performed the DFT calculations. G.D., X. Wang and C.J. synthesized the Li(Fe,Co)As samples. P.Z. performed the ARPES measurements on Fe(Te,Se) and analysed the data with help from Y.I., K.Y., C.B., K. Kuroda, T. Kondo, K.O., K.S., S.W., K.M., T.O., H.D. and S.S.. P.Z., Y.K. and K. Kindo performed the magnetoresistance measurements on Fe(Te,Se). Z.W., X.Wu, R.T., T. Kawakami and M.S. performed the theoretical calculations on Fe(Te,Se). G.D.G., Y.S. and T.T. synthesized the Fe(Te,Se) samples. All authors discussed the manuscript. P.Z. and S.S. supervised the whole project.

Competing interests

The authors declare no competing interests.

Additional information

Supplementary information is available for this paper at https://doi.org/10.1038/s41567-018-0280-z.

Reprints and permissions information is available at www.nature.com/reprints.

Correspondence and requests for materials should be addressed to P.Z. or S.S.

Publisher's note: Springer Nature remains neutral with regard to jurisdictional claims in published maps and institutional affiliations.

Methods

High-quality single crystals of $LiFe_{1-x}Co_xAs$ were synthesized by the self-flux method. The Fe(Te,Se) single crystals of sample #1 were grown by the self-flux method. The composition is $Fe_{1+y}Te_{0.57}Se_{0.43}$, with $y = 14\%$, as detected by the inductively coupled plasma (ICP) atomic emission spectroscopy. The as-grown Fe(Te,Se) single crystals were annealed in a controlled amount of O_2 to remove excess Fe[51]. The Fe(Te,Se) single crystals of sample #2 were grown by the Bridgman technique, with a composition of $FeTe_{0.55}Se_{0.45}$. The as-grown single crystals contain no or very small amounts of excess Fe. No annealing process was applied to sample #2 (ref. [52]). Both Fe(Te,Se) samples show a T_c of ~14.5 K and the same band structure.

The high-resolution ARPES measurements on Li(Fe,Co)As were performed on a spectrometer with a VG-Scienta R4000WAL electron analyser. The energy resolution of the system was set to ~5 meV. The spin-resolved ARPES (SARPES) measurements on Li(Fe,Co)As were carried out with a ScientaOmicron DA30-L analyser, together with twin very-low-energy electron diffraction (VLEED) spin detectors[30]. The energy resolution for the spin-resolved mode was set to ~6 meV for the $x = 3\%$ and 9% samples, and ~12 meV for the $x = 12\%$ sample, with a momentum resolution of ~0.01 $Å^{-1}$. All the ARPES measurements on Li(Fe,Co)As were carried out with a 6.994-eV laser. The same laser SARPES system was used for the high-resolution measurements on Fe(Te,Se). The photon-dependent SARPES measurements on Fe(Te,Se) were carried out at BL9B and HiSOR. The resolution is set to ~6 meV for the laser SARPES, and ~30 meV for the SARPES at HiSOR.

The measurements on Fe(Te,Se) of the in-plane magnetoresistance $\rho(H)$ in static magnetic fields up to 14 T were carried out with a commercial Physical Property Measurement System (PPMS). The measurements in pulsed high magnetic fields up to 30 T were performed with a four-probe point contact method. The experimental data taken with pulsed magnetic fields were recorded on a 16-bit digitizer and analysed using a numerical lock-in technique.

The density functional theory (DFT) calculations employed the projector augmented wave method encoded in the Vienna ab initio simulation package[53–55], and the local density approximation for the exchange correlation functional was used[56]. Throughout this work, a cutoff energy of 500 eV was taken when expanding the wavefunctions into the plane-wave basis. In the calculation, the Brillouin zone was sampled in k space within the Monkhorst–Pack scheme[57]. The number of k points chosen depends on the material: $11 \times 11 \times 5$ and $9 \times 9 \times 9$ for LaOFeAs, LiFeAs, Fe(Te,Se) conventional cells and the $BaFe_2As_2$ primitive cell, respectively. The spin–orbit coupling was included in self-consistent calculations of the electronic structure. The surface spectrum was computed by the surface Green's function method. We note that the dynamical mean-field theory (DMFT) calculations on Fe(Te,Se) show similar band inversion to the DFT calculations[5]. The band inversion in the calculations is unlikely to vanish when taking correlation effects into consideration.

The effective Hamiltonian for the theoretical calculations on Fe(Te,Se) was built on the eight bands (p_z, d_{xy}, d_{yz}/d_{xz}) at the Γ point. First, we derived the four-band model without spin–orbit coupling. The first-principles calculations indicate the four characteristic bands are labelled as the irreducible representations Γ_2^-, Γ_5^+ and Γ_4^+ of the point-group D_{4h} at Γ without spin–orbit coupling. The 4-band time-reversal-invariant $\mathbf{k}\cdot\mathbf{p}$ model was established under the basis of those irreducible representations. Then, the spin-orbit coupling was taken into consideration, by doubling the basis with the spin degree of freedom and introducing additional terms. The (001) surface spectrum was computed by the surface Green's function method. More details can be found in Supplementary Information Part 5.

Data availability

The data that support the findings of this study are available from the corresponding authors upon reasonable request.

References

51. Sun, Y., Taen, T., Tsuchiya, Y., Shi, Z. X. & Tamegai, T. Effects of annealing, acid and alcoholic beverages on $Fe_{1+y}Te_{0.6}Se_{0.4}$. *Supercond. Sci. Technol.* **26**, 015015 (2013).
52. Wen, J., Xu, G., Gu, G., Tranquada, J. M. & Birgeneau, R. J. Interplay between magnetism and superconductivity in iron–chalcogenide superconductors: crystal growth and characterizations. *Rep. Prog. Phys.* **74**, 124503 (2011).
53. Kresse, G. & Hafner, J. Ab initio molecular dynamics for liquid metals. *Phys. Rev. B* **47**, 558–561 (1993).
54. Kresse, G. & Furthmüller, J. Efficiency of ab-initio total energy calculations for metals and semiconductors using a plane-wave basis set. *Comput. Mater. Sci.* **6**, 15–50 (1996).
55. Kresse, G. & Furthmüller, J. Efficient iterative schemes for ab initio total-energy calculations using a plane-wave basis set. *Phys. Rev. B* **54**, 11169–11186 (1996).
56. Perdew, J. P., Burke, K. & Ernzerhof, M. Generalized gradient approximation made simple. *Phys. Rev. Lett.* **77**, 3865–3868 (1996).
57. Monkhorst, H. J. & Pack, J. D. Special points for Brillouin-zone integrations.*Phys. Rev. B* **13**, 5188–5192 (1976).